Master Thesis

Assessment of the Influence of Including Surrounding Tissue in Internal Carotid Artery Biomechanical Modeling

by

Salma EL Kamili

5885388

in partial fulfilment of the requirements of Master of Science in
Biomedical Engineering, Track: Medical Devices
at the Delft University of Technology,
to be defended publicly on Friday 22 November 2024 at 13:45.

TU Delft Supervisor: Prof. dr. ir. Ali Akyildiz
Daily supervisor: Ms Federica Fontana

TU Delft

Abstract

The internal carotid arteries (ICAs) are of vital importance in cerebral blood supply. Hence, accurate modeling of its biomechanical behavior is essential for understanding various pathologies and developing effective treatments. However, computational modeling of the ICA often omits the surrounding tissue environment, which likely limits the accuracy of biomechanical simulations. This study aimed to assess the impact of including surrounding tissues in ICA models on simulation outcomes. Using a single patient-specific ICA geometry, four finite element (FE) models were developed and analyzed: an isolated artery (Model 0), an artery with soft tissue interactions (Model 1), an artery with bone interactions (Model 2), and an artery with both soft tissue and bone interactions (Model 3). The surrounding tissues were modeled using elastic spring elements attached to the outer surface of the arterial wall. Different spring stiffness values were assigned to simulate the distinct properties of surrounding tissues in their corresponding artery segments. Simulations were performed using the FEBio software, the models were analyzed for displacement, stress, and strain distributions. Results showed that surrounding tissues significantly affect arterial biomechanics, with bone having a more dominant effect than soft tissue. The combined tissue model (Model 3) provided the most comprehensive and physiologically accurate representation of the ICA, with a 60.5% reduction in peak displacement, a 6.8% reduction in peak stress, and a 33.0% reduction in peak strain compared to the isolated artery model. However, these preliminary findings using a single ICA geometry prevent us from drawing definitive conclusions. Therefore, our study serves as the groundwork for future investigations and highlights the significance of including surrounding tissues in ICA modeling.

I. Introduction

Cardiovascular diseases (CVDs) represent a major global health burden and account for a substantial proportion of annual mortality. According to the World Health Organization (WHO), CVDs are responsible for 42.5% of all deaths in the European Union (EU), translating to approximately 10,000 deaths per day [1]. This statistic underlines the severe impact of CVDs on public health and the urgent need for effective prevention and treatment strategies. Moreover, CVDs impose a significant economic burden on the EU. Recent estimates indicate that these diseases cost the EU around €282 billion annually. This total includes various cost components, with health and long-term care taking up the largest proportion at €155 billion, which accounts for 55% of all CVD expenses [2]. This financial burden points to the urgent need for improved understanding and management of CVDs.

The internal carotid arteries (ICAs) are vital cardiovascular structures responsible for delivering oxygenated blood to the brain and are subject to several pathologies, including aneurysm formation and atherosclerosis [3]. These conditions pose major challenges for clinicians in terms of diagnosis, treatment planning, and understanding disease progression [4]. As a result, over the last few years, computational models–especially finite element (FE) modeling–have been widely used as a tool to support decision-making and analyze the complex biomechanics of the ICAs [5]–[7].

However, a significant limitation in current modeling approaches is the oversimplification or complete omission of the surrounding tissue environment. The ICA does not exist in isolation; it is embedded within a complex matrix of tissues, including muscles, fascia, and neighboring structures, which can influence its behavior and responses to pathological conditions or interventions [3]. Most existing computational models use simplified meshes and boundary conditions that fail to account for the mechanical properties and constraints imposed by these surrounding tissues. This drawback is apparent in studies that employ isolated artery models (e.g., [8]–[11]). These models focus on analyzing the artery as an isolated structure, often neglecting its interactions with surrounding tissues.

Consequently, this study aims to determine whether incorporating the impact of surrounding tissues in computational models could improve their accuracy and relevance, thereby bridging the gap between simulations and physiological conditions.

A. Anatomy of ICA

The ICAs are the main arteries that supply blood to the brain. There are two internal carotid arteries, one located on the left side and the other on the right side of the neck [12]. The ICA originates from the bifurcation of the common carotid artery (CCA) before entering the skull through the carotid canal, an opening in the temporal bone [13], where it starts a series of turns and eventually bifurcates into the middle and anterior cerebral arteries (MCA and ACA) [14]. Figure 1 illustrates the branching of the CCA into the ICA and the external carotid artery (ECA).

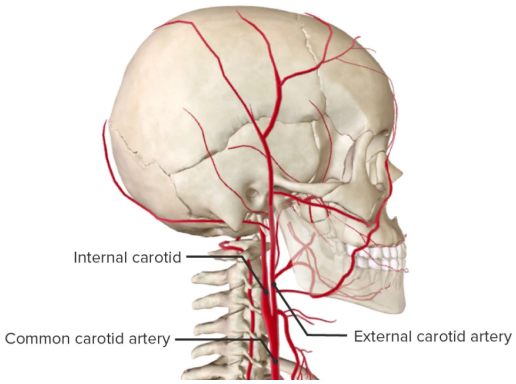

Fig. 1: Lateral view of the neck, showing the origin and bifurcation of the CCA. The CCA is shown ascending through the neck before dividing into the internal and external carotid arteries at the carotid bifurcation [15].

There are several classification systems for categorizing the segments of the ICA [16], [17]. However, in clinical settings, the most commonly used classification is the Bouthillier Classification (1996), also known as the Cincinnati classification. It divides the internal carotid artery into seven segments based on angiographic appearance: C1 cervical; C2 petrous; C3 lacerum; C4 cavernous; C5 clinoid; C6 ophthalmic; and C7 communicating [18], as shown in Figures 2 and 3.

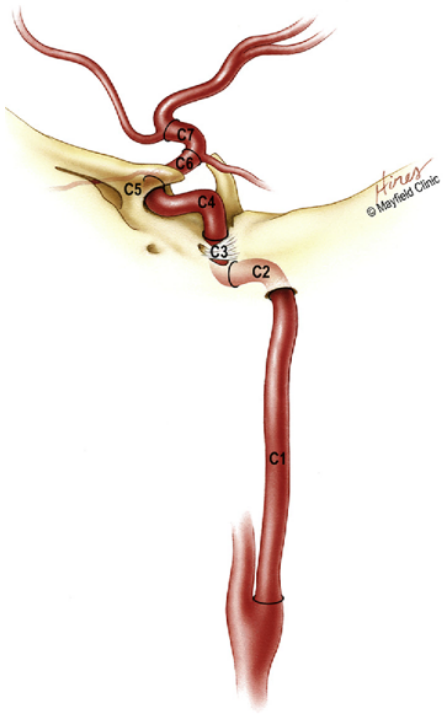

Fig. 2: The seven segments of the ICA as defined by Bouthillier et al. in 1996: C1 cervical; C2 petrous; C3 lacerum; C4 cavernous; C5 clinoid; C6 ophthalmic; and C7 communicating [18], [19].

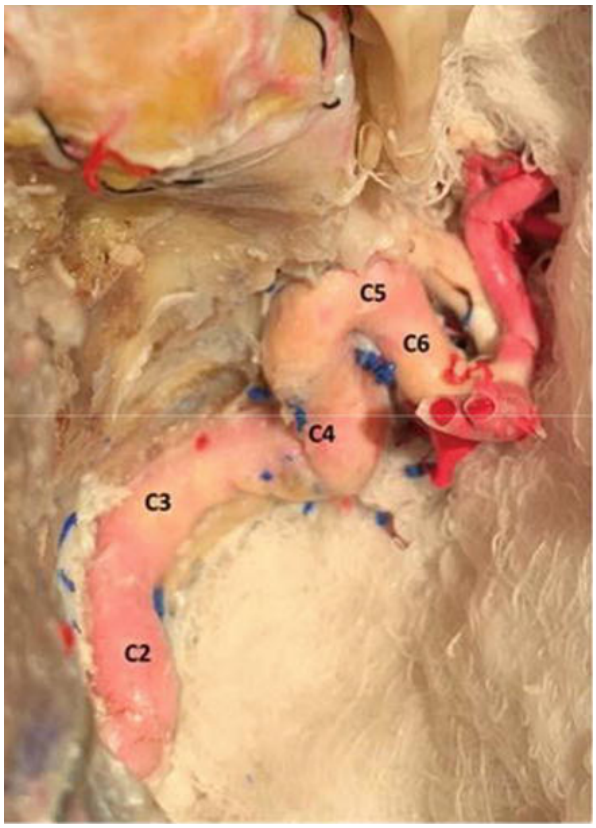

Fig. 3: Photograph of a piece obtained through anatomical dissection showing some of the segments of the ICA [20]. *C2 petrous; C3 lacerum; C4 cavernous; C5 clinoid; C6 ophthalmic.*

Using a numerical system based on blood flow direction, this categorization gives anatomical descriptions of each segment as well as information about the compartments they pass through, covering the whole internal carotid artery [18]. Figure 4 illustrates the seven segments of the ICA and their branches.

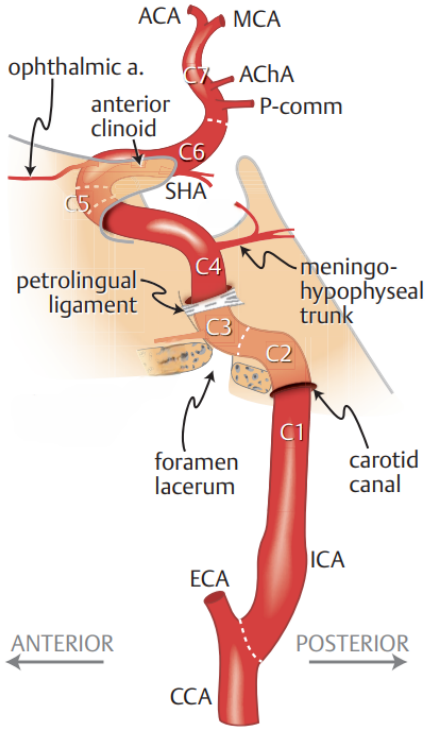

Fig. 4: Schematic drawing of the segments of the ICA and its branches [19]. *ACA = anterior cerebral artery; AChA = anterior choroidal artery; CCA = common carotid artery; ECA = external carotid artery; MCA= middle cerebral artery; P-comm = posterior communicating artery; SHA = superior hypophyseal artery; C1 cervical; C2 petrous; C3 lacerum; C4 cavernous; C5 clinoid; C6 ophthalmic; C7 communicating.*

The Cervical segment (C1) begins from one of the two terminal branches of the CCA between the C3 and C5 vertebral levels [13]. The ICA proceeds upward through the neck without any branching to the entrance of the carotid canal in the temporal bone [3].

The Petrous segment (C2) of the ICA courses through the petrous part of the temporal bone until it reaches the foramen lacerum [12], [21], [22]. This segment gives rise to two branches: the caroticotympanic artery and the vidian artery [3].

The Lacerum segment (C3) is a short segment that extends from the posterior edge of the foramen lacerum to the petrolingual ligament (PLL) [12], [21]. The PPL is located on the wall of the cavernous sinus. It primarily connects the petrous part of the temporal bone (hence ”petro-”) and the lingula of the sphenoid bone (hence ”lingual”) while also serving as an important anatomical landmark for the transition between segments of the internal carotid artery [23].

The Cavernous segment (C4) of the ICA starts at the superior margin of the petrolingual ligament and travels through the cavernous sinus [12], [21], [22]. This segment branches into the meningohypophyseal trunk and the inferolateral trunk [3].

The Clinoid segment (C5) is another short segment that extends from the proximal dural ring (PDR) to the distal dural ring (DDR) [12], [21], [22], as detailed in Figure 5.

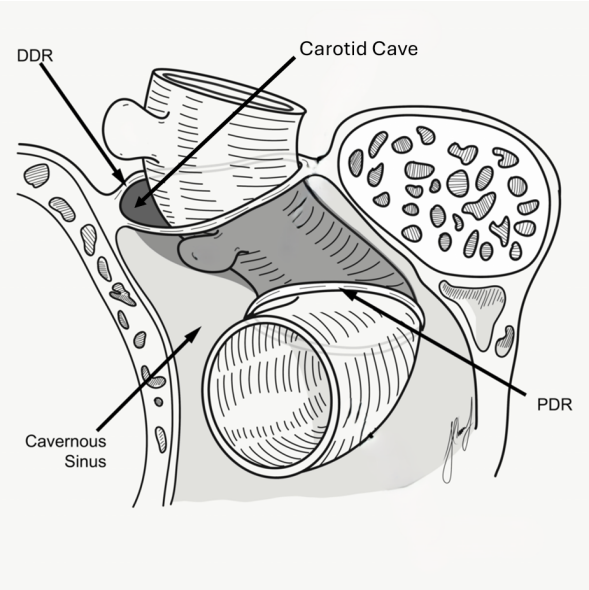

Fig. 5: Anatomic drawing showing the clinoid segment of the ICA. The clinoid (C5) segment of the ICA, emerges from the cavernous sinus at the proximal dural ring (PDR) and extends to the distal dural ring (DDR). The DDR firmly attaches to the adventitia of the lateral aspect of the ICA but is redundant on the medial aspect, which forms the potential space of the carotid cave [24].

The Ophthalmic segment (C6) of the ICA begins at the DDR and ends just proximal to the origin of the posterior communicating artery [12], [21]. Its branches include the ophthalmic artery and the superior hypophyseal artery (SHA) [3].

The Communicating (terminal) segment (C7) starts from the proximal origin of the posterior communicating artery and ends at the ICA's bifurcation into the anterior cerebral artery (ACA) and the middle cerebral artery (MCA) [12], [21], [22]. The branches of this segment include the posterior communicating artery (P-comm), anterior choroidal artery (AChaA), anterior cerebral artery (ACA), and middle cerebral artery (MCA) [3].

Table I provides a general overview of the tissues surrounding each segment of the ICA. The ICA is surrounded by different types of tissues as it travels from the neck into the skull and ultimately to the brain. The surrounding tissues change as the artery passes through different anatomical regions, from the soft tissues of the neck to the bony structures of the skull base and finally the meninges and brain tissue [3], [19].

TABLE I: Surrounding Tissues of the ICA Segments [3], [19].

ICA Segment	Surrounding Tissues
Cervical (C1)	- Carotid sheath (connective tissue) - Neck muscles (muscular tissue)
Petrous (C2)	- Petrous part of temporal bone (osseous tissue) - Dura mater (connective tissue)
Lacerum (C3)	- Fibrocartilaginous tissue - Petrolingual ligament (connective tissue)
Cavernous (C4)	- Venous blood (cavernous sinus) - Dura mater (connective tissue)
Clinoid (C5)	- Dural rings (connective tissue) - Anterior clinoid process (osseous tissue)
Ophthalmic (C6)	- Subarachnoid space (cerebrospinal fluid) - Meninges (connective tissue)
Communicating (C7)	- Brain parenchyma - Subarachnoid space (cerebrospinal fluid) - Meninges (connective tissue)

B. Finite Element Method

The finite element method (FEM) is a powerful tool in biomechanical research. It is a numerical method used to analyze complex physical systems by breaking down large structures into finite, smaller, simpler elements (hence, the name finite elements) [25]. It has become one of the most widely used methods for structural analysis of soft arterial tissues [26]. Therefore, in the context of our study, FEM provides a strong framework to model and understand the mechanical behavior of both the artery and its surrounding tissues. By discretizing the ICA and its environment into a mesh of finite elements, FEM provides a detailed analysis of strain and stress distributions that occur due to various physiological and pathological loads [26]. This method has proven to be quite effective in capturing the complex, non-uniform mechanical properties of biological tissues, which often exhibit nonlinear and anisotropic behavior [5]. Additionally, FEM's flexibility in defining boundary conditions and material properties that reflect the heterogeneous nature of biological systems leads to accurate simulations that mimic physiological conditions [27]. Therefore, FEM is a useful tool to predict how the surrounding tissues mechanically interact with the ICA and to identify regions of potential risk to prevent the development of pathologies [28].

In addition to structural simulations, Fluid-Structure Interaction (FSI) simulations integrate both the structural mechanics of the arterial wall and the hemodynamics of blood flow to provide a realistic representation of how blood flow affects arterial deformation. This approach reveals insights into hemodynamics, wall stresses, and cardiovascular disease progression [29]. Furthermore, the integration of FSI simulations in ICA studies is relevant for investigating the impact of surrounding tissue properties on arterial biomechanics. By incorporating the surrounding tissues, as investigated in this thesis, FSI models can deliver accurate predictions of ICA deformation and stress distributions under pulsatile blood flow conditions. This advanced modeling approach can lead to improved risk assessments and diagnostic accuracy for

various ICA pathologies, and provide surgeons with insights that assist in their treatment decisions.

C. Thesis objective, Research question, and Outline

Despite advances in medical imaging and computational modeling, a comprehensive understanding of how the surrounding tissue affects the biomechanical response of ICAs is still limited. This is because current computational models of cerebral arteries often do not consider the surrounding tissue environment, as their incorporation would require additional computational resources [30]. Hence, these models focus primarily on the fluid dynamics within the arterial lumen and the mechanical properties of the arterial wall, as well as the characteristics of plaque components when present (e.g., [8]–[11], [31]–[33]). The objective of this study is to develop a more comprehensive computational model of the ICA that incorporates the presence of surrounding tissues. By comparing this enhanced model with existing simplified approaches, we aim to quantify the impact of external tissue on simulation results and assess its significance in improving the accuracy of ICA modeling for clinical applications. Thus, the main research question of this master thesis is:

"How does the inclusion of surrounding tissue in computational models of the internal carotid artery affect simulation outcomes?"

This research is structured as follows: Section II details the methodology employed, including data acquisition, patient-specific model construction, and the implementation of surrounding tissues in the computational models created. Section III presents the results obtained from the simulations, comparing the outcomes of models with and without surrounding tissue. Section IV offers a comprehensive discussion of the results, analyzing their implications for ICA modeling and potential clinical applications. This section also addresses the limitations of the study and suggests directions for future research in this field. Finally, Section V concludes the thesis by summarizing the main findings.

II. Methods

A. Data Acquisition

Patient data was obtained from one clinical study, the prospective multicenter 'Plaque At RISK' (PARISK) cohort study. A total of 244 patients were selected for the PARISK cohort, all of whom had recently experienced a transient ischemic attack (TIA) or minor stroke due to ischemia in the territory of a carotid artery, diagnosed within three months of symptom onset and with non-severe stenosis (less than 70%) at baseline. Out of these patients, 199 underwent baseline multi-detector computed tomography angiography (MDCTA) imaging with a specific focus on the carotid bifurcation; however, the scans also covered the head and included the ICA. Institutional Review Board approval was obtained and all patients gave written informed consent. The study protocol conformed to the ethical guidelines of the 1975 Declaration of Helsinki and had been priorly approved by the ethics committees of the research centers participating in the study. An in-depth description of the study design has previously been described in the study-design article [34]. Imaging acquisition was performed using either a 16-, 64- or 128-slice multi-detector row CT system through a standardized optimized contrast-enhanced protocol.

B. Patient-Specific Model Construction

In the process of constructing a geometrical model of the ICA, as depicted in Figure 6, a combination of advanced imaging techniques and computational methods are employed to accurately represent the artery's geometry. The 3D geometry of the lumen and calcifications are obtained through careful segmentation of MDCTA images. This segmentation process is carried out using a hybrid approach that combines ITK-SNAP and 3D Slicer software tools, which allow for precise identification of the arterial lumen and any calcified regions. To model the arterial wall, the segmented lumen geometry is extruded with a uniform thickness of 0.5 mm. Although calcifications were not directly considered in the analysis of results, they were included in the model to maintain anatomical accuracy and reflect the patient's specific condition. Moreover, the presence of calcification in the model can be adapted for various research questions in future work related to blood flow dynamics or wall stress distributions.

C. Meshing

Initial triangular surface meshes in STL format were refined using the Geogram library, specifically the *ggremesh* function in MATLAB [35]. The element size was set to 0.3 mm for the vessel wall, whereas a finer resolution of 0.2 mm was applied for calcified areas to better capture their complex geometry. The main type of element that has been widely used for modeling arterial walls is tetrahedral [36]. Complex and irregular geometries of arterial walls, such as bifurcations and curved sections, are frequently represented by tetrahedral elements [37], [38]. For patient-specific models, tetrahedral elements are often preferred due to their ability to generate high-quality meshes quickly (highly automated) and their geometric flexibility [39]. Therefore, for the volumetric mesh generation of our model, we employed TetGen, a tetrahedral meshing tool developed by the Weierstrass Institute for Applied Analysis and Stochastics (WIAS) [40], [41]. TetGen was accessed through the GIBBON toolbox in MATLAB, which provides a convenient interface for generating and modifying meshes [42]. TetGen generated linear tetrahedral elements throughout the model volume. Figure 7 represents the surface mesh composed of triangular elements evenly distributed along the artery.

For the FE analysis of our model, we are using FEBio (Finite Elements for Biomechanics) [43] as the primary software tool. It is an open-source that is designed for nonlinear finite element analysis in biomechanics and biophysics. It provides modeling scenarios, constitutive models, and boundary conditions relevant to different areas in biomechanics [44]. To conduct the analysis, it is important to assign appropriate boundary conditions and material properties to the components of the FE model. Boundary conditions define the constraints and external forces acting on the model, while material properties determine how the model responds mechanically to those conditions. For biological tissues, which often exhibit complex and nonlinear behavior, hyperelastic models are frequently employed to accurately represent their material characteristics.

D. Hyperelastic Models

1) Neo-Hookean Model

The Neo-Hookean model is a simplified hyperelastic material model commonly used to describe the nonlinear stress-strain behavior of rubber-like substances and some biological tissues [45]. The Neo-Hookean model is an extension of Hooke's law in the case of large deformations [46]. Hooke's Law describes the linear relationship between stress and strain in elastic materials. It states that the amount of deformation (strain) of an elastic material is directly proportional to the applied load (stress) within the material's elastic limit [47]. Hooke's Law can be expressed as [48]:

$$\sigma = E \cdot \varepsilon \tag{1}$$

Where:

- σ = stress (force per unit area)
- E = modulus of elasticity (Young's modulus)
- ε = strain (relative deformation)

In the initial loading range, the stress-strain behavior is often linear (similar to Hooke's Law). As the material is further deformed, it enters a nonlinear regime which the Neo-Hookean model captures [49]. The strain energy density function for an incompressible Neo-Hookean material is as follows [50]:

$$W = C_1(I_1 - 3) \tag{2}$$

Where:

- W: strain energy density

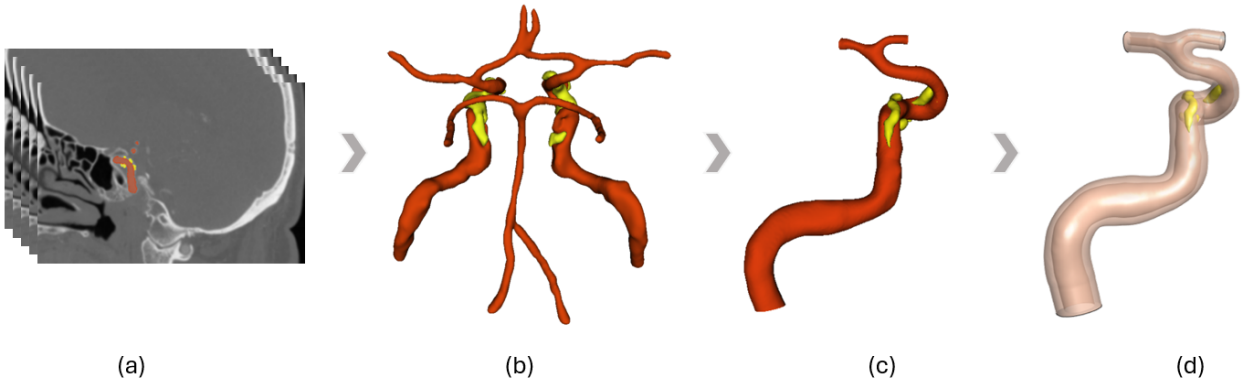

Fig. 6: Geometrical model construction process for the ICA. a) Top view of MDCTA image stack showing the ICA segmentation process. b) 3D model of the main intracranial arteries (highlighted in red) and their calcifications (highlighted in yellow) obtained through segmentation in ITK snap and 3D slicer. c) Refined 3D model of the left ICA and its calcifications, achieved through cropping and smoothing techniques during post-processing. d) 3D model of the arterial wall generated in Matlab through homogeneous extrusion of the lumen.

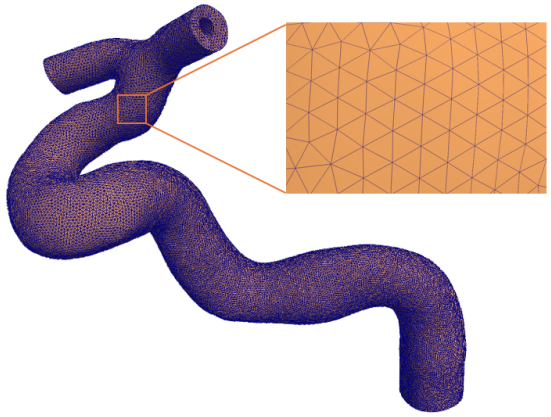

Fig. 7: Zoomed-in view of the triangular surface mesh used for modeling the arterial wall of the ICA.

- C_1: material constant
- I_1: first invariant of the left Cauchy-Green deformation tensor

2) *Mooney-Rivlin Model*

The Mooney-Rivlin model is a widely used hyperelastic material model in continuum mechanics, particularly for modeling rubber-like materials and soft tissues [45]. The Mooney-Rivlin model can be viewed as an extension of the Neo-Hookean model, by adding a second component: the second invariant of the left Cauchy-Green strain tensor [51]. This model defines the strain energy density function as a linear combination of two invariants of the left Cauchy-Green deformation tensor. For an incompressible material, the strain energy density function is given by [50]:

$$W = C_1(\bar{I}_1 - 3) + C_2(\bar{I}_2 - 3) \tag{3}$$

where:

- W: Strain energy density per unit volume.
- C_1 and C_2: Material constants.
- $\bar{I}_1$ and $\bar{I}_2$: The first and second invariants of the deviatoric part of the deformation tensor.

3) *Ogden Model*

The Ogden model is a hyperelastic material model used to describe the nonlinear stress-strain behavior of complex materials like rubber, polymer, and biological tissues [52]. This model is expressed in terms of the principal stretches, rather than the strain tensor invariant like in the Mooney-Rivlin and Neo-Hookean models [53]. The strain energy density function for an incompressible material is as follows [54]:

$$W = \sum_{n=1}^{N} \frac{\mu_n}{\alpha_n} \left(\lambda_1^{\alpha_n} + \lambda_2^{\alpha_n} + \lambda_3^{\alpha_n} - 3\right) \tag{4}$$

Where:

- N: the order of the model.
- μ_n and α_n: Material constants.
- λ_1, λ_2, λ_3: Principal stretches of the material.

E. Material Properties

The model consisted of two key components: arterial wall and calcification.

Vascular calcification is usually assumed to exhibit nonlinear, incompressible, and isotropic behavior [55]–[57]. It was modeled using the Neo-Hookean model (Equation 2). The arterial wall was modeled as a nonlinear and incompressible material using the Ogden model (Equation 4).

Given the use of FEBio [43], the material type for calcification was set as *Mooney-Rivlin*. By setting C_2 = 0 in Equation 3, the model is reduced to an uncoupled version of the Neo-Hookean constitutive model [58]. The material type for the arterial wall was set as *Ogden*.

The equations presented below are defined according to the FEBio software documentation [46].

For Mooney-Rivlin models, the following three material parameters must be defined:

- c_1: Coefficient of the first invariant term.
- c_2: Coefficient of the second invariant term.
- k: Bulk modulus.

The strain-energy function is given by:

$$\Psi = C_1 \left(\tilde{I}_1 - 3\right) + C_2 \left(\tilde{I}_2 - 3\right) + \frac{1}{2} K \left(\ln J\right)^2 \quad (5)$$

Where:

- C_1 and C_2: Material constants.
- $\tilde{I}_1$ and $\tilde{I}_2$: First and second invariants of the deviatoric right Cauchy-Green deformation tensor $\tilde{C}$.
- K: Bulk modulus.
- J: Determinant of the deformation gradient tensor.

For Ogden Models, the following material parameters must be defined:

- $c[n]$: Coefficient of n^{th} term (where n can range from 1 to 6).
- $m[n]$: Exponent of n^{th} term (where n can range from 1 to 6).
- k: Bulk modulus.

The strain energy function for this material is given in terms of the eigenvalues of the deformation tensor:

$$\Psi = \sum_{i=1}^{N} \frac{c_i}{m_i^2} \left(\tilde{\lambda}_1^{m_i} + \tilde{\lambda}_2^{m_i} + \tilde{\lambda}_3^{m_i} - 3\right) + U(J) \quad (6)$$

Here, $\tilde{\lambda}_i^2$ are the eigenvalues of $\tilde{C}$, c_i, and m_i are material coefficients, N ranges from 1 to 6, $U(J)$ is the volumetric component and J is the determinant of the deformation gradient.

Table II represents the parameter settings used in this study. The material properties of the arterial wall and calcification were based on the findings of Moerman et al. and Monson et al. [11], [59], [60].

TABLE II: Material parameters on FEBio.

Arterial Wall		Calcification	
Model type	Ogden	Model type	Mooney-Rivlin
Density	1000 kg/m3	Density	1000 kg/m3
Bulk modulus	4.16 MPa	Bulk modulus	13.3 MPa
c1	0.2 MPa	c1	1.6 MPa
c2	0.2 MPa	c2	0
m1	2		
m2	-2		

F. Boundary and Loading conditions

To accurately simulate the vessel wall's behavior under physiological conditions in a simplified yet effective way, two key boundary conditions were implemented in our model:

- Zero displacement at both the inlet and outlet.
- Internal pressure load.

The zero displacement condition at the inlet and outlet (Figure 8) fixes these ends of the vessel in space, preventing any rigid body motion, from a compatibility point of view.

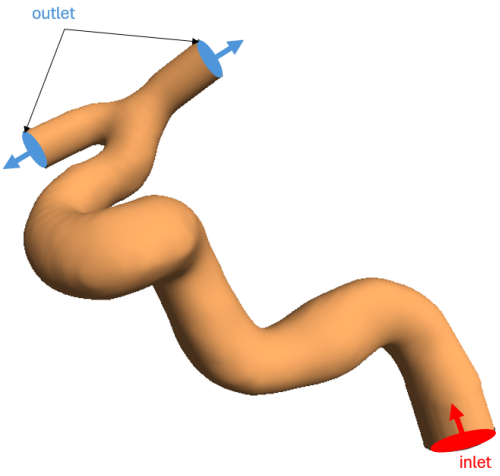

Fig. 8: The locations of the inlet (denoted by the red plane) and outlets (denoted by the blue planes) in the ICA model.

This constraint mimics the anatomical attachment of blood vessels to surrounding tissues and helps ensure model stability during simulation. This was achieved by constraining all degrees of freedom, using the *zero displacement* boundary condition in FEBio [46].

The internal pressure load applied to the luminal (inner) surface of the artery, represents the blood pressure exerted on the vessel wall, which is the primary force causing vessel deformation under normal physiological conditions [61].

In FEBio [46], pressure loads are defined using the *pressure* boundary condition. A pressure load of 120 mmHg was applied using a load curve, a common approach for defining time-dependent boundary conditions [62]. Figure 9 represents the Pressure Load curve.

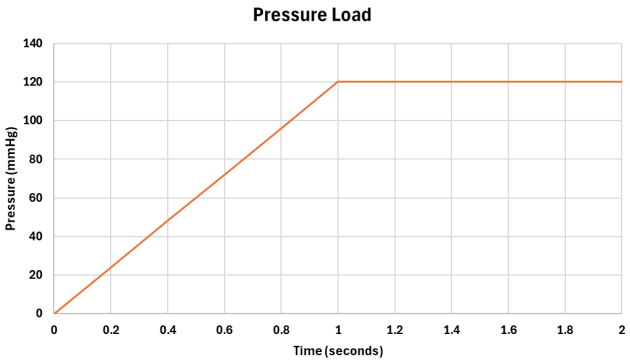

Fig. 9: Pressure Load curve. This graph shows the progression of a pressure load applied to the inner surface of the artery over a 2-second simulation. The x-axis represents time and the y-axis represents the pressure magnitude. The load starts at zero, indicating no pressure applied initially. As time progresses to 1 second, it increases linearly to reach a value of 120 mmHg, after which it remains constant. This linear increase reflects a gradual application of pressure, followed by a sustained load of 120 mmHg.

The linear ramp-up phase facilitates a smooth transition from the unloaded to the fully loaded state, while the constant phase maintains the maximum pressure for the remainder of

the analysis. This gradual application represents how pressure builds up over time rather than being applied instantaneously.

G. Surrounding Tissues

The surrounding tissues of arteries, including both osseous and soft tissue structures, contribute significantly to external support and influence the biomechanical behavior of the vessels during hemodynamic processes. This external support system acts as a natural constraint by providing structural support, resisting deformation, and absorbing mechanical energy, which helps arteries withstand internal pressures and maintain their shape during blood flow [63], [64]. To accurately simulate this interaction, Moireau et al. [64] applied a boundary condition using a generalized Robin condition, which combines stress, displacement, and velocity to capture the complex mechanical relationship between the artery and its surroundings. The Robin condition incorporates both the elastic and viscoelastic properties of the external tissues, allowing the model to mimic their dynamic response [65]. The following Robin boundary conditions were enforced on the outer arterial wall Γ_s:

$$\underline{\underline{\sigma}}_s \cdot \underline{n}_s = -k_s \underline{y}_s - c_s \underline{u}_s - p_0 \underline{n}_s, \quad \text{on } \Gamma_s. \tag{7}$$

Where:

- σ_s: the stress on the arterial wall.
- n_s: the normal vector to the boundary.
- k_s and c_s are parameters that model the elastic and viscoelastic responses of the external tissue, respectively.
- y_s: the displacement of the tissue.
- u_s: the velocity.
- p_0: the external pressure acting on the tissue boundary.
- Γ_s: the surface where these conditions apply.

In our implementation of the Robin boundary condition to model the external tissue support, we have chosen to focus solely on the elastic component, omitting the viscoelastic and pressure elements. This can be justified based on several key factors.

Firstly, using an elastic model for bone and soft tissue simplifies the computational complexity and preserves the mechanical behavior of these structures. Bone, in particular, exhibits primarily elastic properties under physiological loading conditions [66]. For soft tissues, while they do exhibit viscoelastic properties, the elastic component often dominates their response to the relatively rapid deformations associated with blood flow [67].

Secondly, blood flow dynamics typically occur on a relatively rapid timescale. The pulsatile nature of blood flow causes tissues surrounding blood vessels to deform rapidly, usually within fractions of a second. At these short timescales, the instantaneous elastic response of the bone and soft tissues tends to dominate over their time-dependent viscoelastic behavior [68].

Lastly, the pressure component of the Robin condition may be less significant for modeling the surrounding tissues in many blood flow scenarios, as the primary interaction between the vessel and its environment is often mechanical rather than pressure-based [69], [70].

To summarize, the focus on the elastic component can capture the most relevant aspects of tissue-vessel interaction while maintaining model simplicity and computational efficiency. This simplification can increase the accuracy in simulations involving patient-specific models, where detailed tissue properties may not be available [71].

To accurately model the external support provided by surrounding tissues, a specialized approach is required within the FEBio software framework [46]. We implemented this approach using a custom MATLAB code interfaced with FEBio. The process begins by extruding nodes from the existing artery wall mesh to create new endpoint nodes for the springs. These extruded nodes are then incorporated into the mesh structure using the *cat* function, which allows for absolute concatenation of the new nodes with the existing mesh nodes. It is important to note that while these new nodes are added to the mesh, they are not used in defining any finite elements and do not form part of the finite element structure itself. The springs are then defined as discrete elements, connecting the original mesh nodes to their corresponding extruded nodes. To simulate the constraining effect of external tissue, a *zero displacement* boundary condition is applied to the extruded nodes, limiting their displacements. The material properties of the springs are defined using FEBio's *discrete material* element by employing linear spring characteristics to represent the elastic behavior of the external tissue.

The elastic support boundary conditions for the arterial wall were implemented using different parameter values for two distinct regions based on the surrounding tissue types: bone and soft tissue (listed in Table III [64]). These regions were defined along the internal carotid artery (ICA) following the Bouthillier classification of ICA segments [18].

TABLE III: External tissue support parameters (units: cgs) [64]

Region	Bone	Soft tissue
k_s	10^7	10^3

The bone region corresponds to the petrous (C2) and lacerum (C3) segments of the ICA, where the artery passes through the temporal bone and carotid canal. Additionally, the clinoid (C5) segment passes under the anterior clinoid process, which is a bony prominence of the sphenoid bone [72]. The soft tissue region covers the remaining segments, including the cervical (C1), cavernous (C4), ophthalmic (C6), and communicating (C7) segments.

Figure 10 illustrates the ICA and the surrounding tissues' regions. The bone regions were first identified, because they serve as easily identifiable landmarks in the anatomy of the ICA, and the remaining regions were assigned to the soft tissues.

H. Bone Interaction

In modeling the interaction between the ICA and surrounding bone, we chose to directly attach the bone springs to

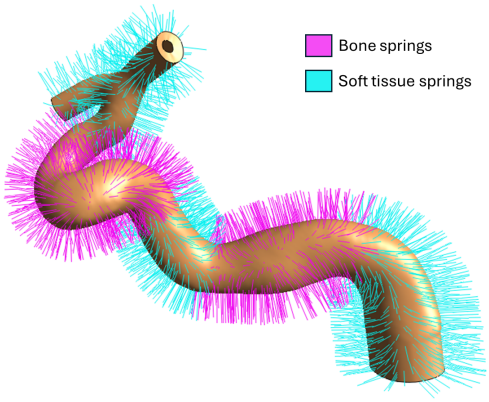

Fig. 10: 3D Model of the ICA with the presence of surrounding tissues, which are represented using spring elements.

the artery, despite a small gap that typically exists between the artery and bony structures. This decision was made to simplify the model while maintaining the mechanical constraints imposed by the bone. The small space, as shown in Figure 11, between the artery and bone is generally filled with connective tissue or minor tissue that provides minimal mechanical resistance [73].

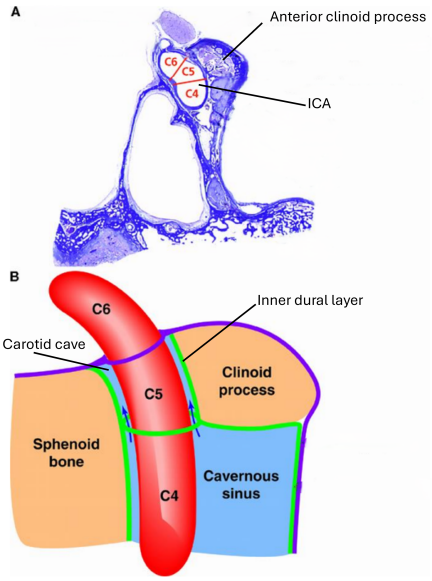

Fig. 11: A: Coronal histological section highlighting the small gap around the clinoid segment of the ICA. B: Schematic drawing illustrating the small space between the inner dural layer and the clinoid ICA [73], [74]. *C4 cavernous; C5 clinoid; C6 ophthalmic.*

Thus, for the purposes of our simulation, this gap was considered negligible, and the bone springs were attached directly to the artery to reflect the dominant mechanical influence of the surrounding bone without overcomplicating the model unnecessarily.

I. Biomechanical Metrics

In the analysis of our FEBio model simulation results, we focused on three fundamental biomechanical metrics: stress, strain, and displacement.

In FEBio [46], these metrics are defined as follows:

Displacement Magnitude is a nodal variable that represents the total movement of a node from its original position. It is automatically computed by FEBio as the Euclidean norm of the displacement vector components (x, y, and z) [75].

Effective Stress, also known as von Mises stress, is an element variable that provides a scalar representation of the stress state. It is derived from the Cauchy stress tensor, which describes the internal forces acting within a material under deformation. [75]–[77].

Effective Lagrange Strain is an element variable that represents the deformation of a material compared to its original form. It is calculated using the Green-Lagrange strain tensor, which is a material tensor that provides insight into the material's deformation relative to its undeformed state [75], [78].

III. Results

A. The Created Models

In this thesis, four FE models of the ICA were developed to assess the influence of the individual and combined effects of surrounding tissues (soft tissue and bone) on simulation results and evaluate its significance in improving the accuracy of ICA modeling for clinical applications. These models, as illustrated in Figure 12, were constructed with increasing complexity to capture the interaction between the artery and its environment, starting from a simplified baseline and incorporating various tissue representations.

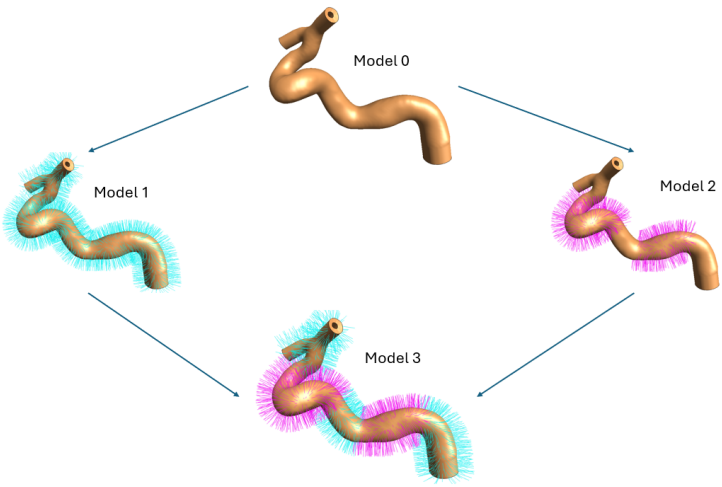

Fig. 12: The progressive addition of surrounding tissues from Model 0 to Model 3. Model 0 serves as the baseline with no surrounding tissue. Models 1 and 2 each provide incremental improvements by isolating the effects of soft tissue (represented by blue springs) and bone (represented by pink springs), respectively. Model 3 combines both tissues for a more realistic and comprehensive simulation.

1) Model 0 - Isolated Artery/Baseline: Our initial model, referred to as Model 0, represented the ICA as an isolated structure without any surrounding tissue. This simplified approach, commonly used in existing literature that focuses solely on the artery itself, serves as a baseline for comparison. However, this model lacks the external support and constraints present in vivo.

2) Model 1 - Soft Tissue Interaction: Building upon the baseline, Model 1 incorporated soft tissue springs around the entire artery. This addition was motivated by the need to account for the supportive and constraining effects of surrounding soft tissues, such as muscles and connective tissues. The inclusion of these springs represents a more realistic physiological scenario, as the ICA does not exist in isolation within the body.

3) Model 2 - Bone Interaction: Model 2 focused on the unique anatomical relationship between the ICA and adjacent bony structures. In this model, stiffer bone springs are implemented in areas where the artery is in close proximity to or passes through bony channels to simulate the rigid mechanical constraints imposed by bone. This modification aimed to examine how the presence of bone affects the artery's mechanical response.

4) Model 3 - Combined Soft Tissue and Bone Interaction: The final model, identified as Model 3, represented the most comprehensive and physiologically accurate representation of the ICA. This model combined the features of Models 1 and 2, incorporating both soft tissue springs and bone springs in their respective anatomical regions. By integrating these elements, we aimed to create a holistic model that approximates the complex mechanical environment of the ICA in vivo.

The progressive modeling approach was chosen to systematically isolate and study the impact of each type of surrounding tissue on the ICA. By first analyzing the effects of soft tissue (Model 1) and bone (Model 2) individually, we can gain a clearer understanding of the specific mechanical influences of each tissue type. Additionally, Model 3, which combines both soft tissue and bone, delivers a more realistic representation of the artery's interactions.

B. *Displacement Magnitude*

The displacement results, evaluated at the last time point (1 second), for all four models are presented in Figures 13–16. Model 0, which serves as the baseline without surrounding tissue, exhibited the highest peak displacement of 0.82 mm (Figure 13). The incorporation of soft tissue in Model 1 reduced the peak displacement to 0.60 mm (Figure 14), while the isolated effect of bone in Model 2 further decreased it to 0.34 mm (Figure 15). Model 3, combining both soft tissue and bone, demonstrated the lowest peak displacement of 0.32 mm (Figure 16).

Furthermore, the locations of maximum and minimum displacements varied across the models, as shown in Figure 17. Models 2 and 3 showed both their maximum and minimum displacements in the soft tissue area. In contrast, while Models 0 and 1 shared the same location for minimum displacement, their maximum displacement locations differed from Models 2 and 3, as well as from each other.

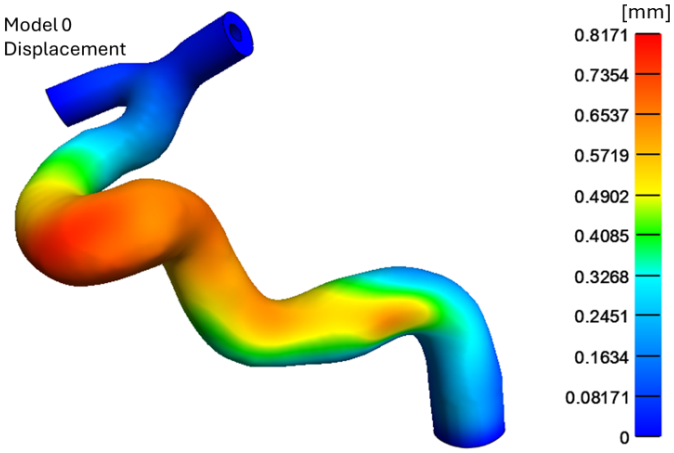

Fig. 13: Displacement results for Model 0. Peak displacement at t=1s: 0.82 mm.

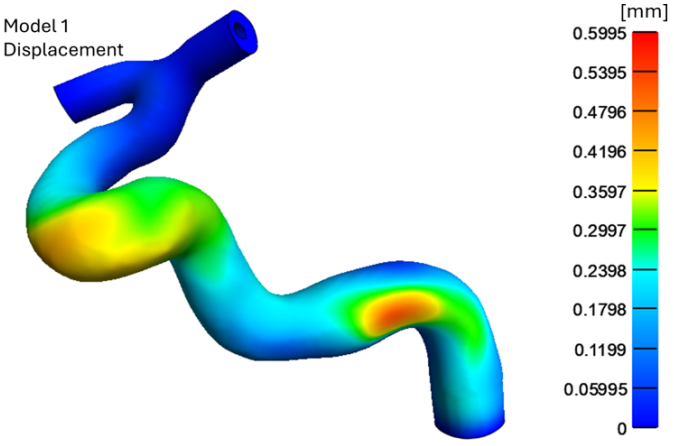

Fig. 14: Displacement results for Model 1. Peak displacement at t=1s: 0.60 mm.

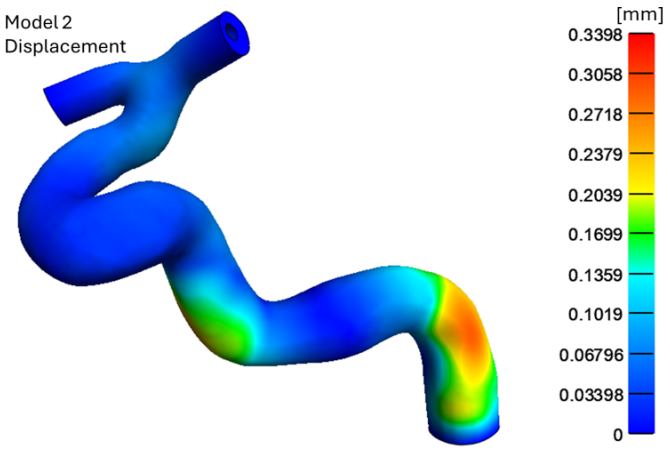

Fig. 15: Displacement results for Model 2. Peak displacement at t=1s: 0.34 mm.

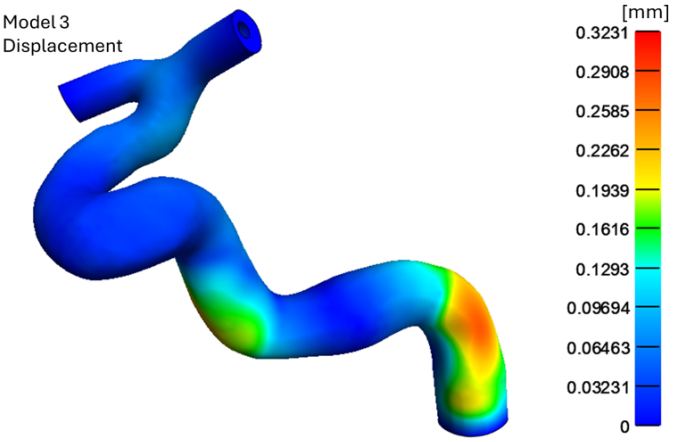

Fig. 16: Displacement results for Model 3. Peak displacement at t=1s: 0.32 mm.

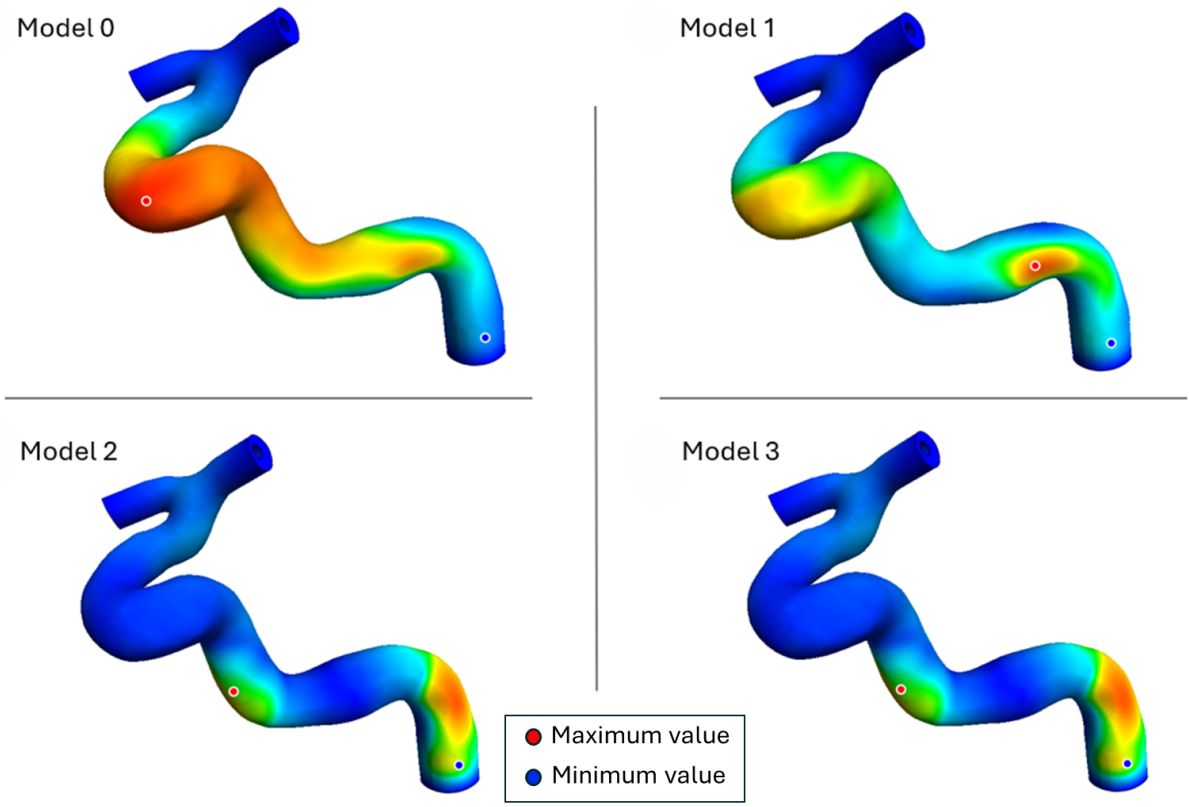

Fig. 17: The location of maximum and minimum displacements across all models, at t=1s.

C. *Effective Stress*

The stress analysis results for the four models revealed distinct variations in peak stress values, as illustrated in Figures 18–21, all assessed at the final time point (1 second). Model 0, which serves as the isolated artery, showed a peak stress value of 0.15 MPa (Figure 18). Model 1, incorporating soft tissue, achieved a higher peak stress of 0.18 MPa (Figure 19). Model 2, isolating the effects of bone tissue, recorded a lower peak stress of 0.14 MPa (Figure 20), compared to Model 1. Model 3, which integrates both soft and bone tissue, displayed the lowest peak stress at 0.14 MPa (Figure 21).

Regarding the location of maximum and minimum stresses, as depicted in Figure 22, Model 0 and Model 1 exhibit both their maximum and minimum stress values at the same locations, indicating similar stress distribution patterns in these models. On the other hand, Model 2 and Model 3 share common locations for their minimum and maximum stress values.

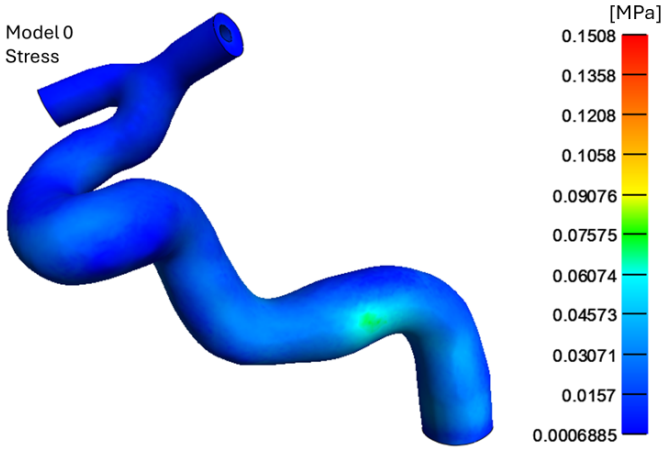

Fig. 18: Stress results for Model 0. Peak stress at t=1s: 0.15 MPa.

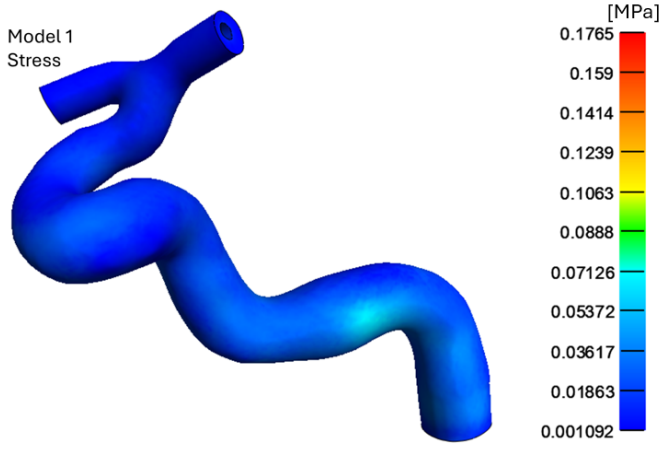

Fig. 19: Stress results for Model 1. Peak stress at t=1s: 0.18 MPa.

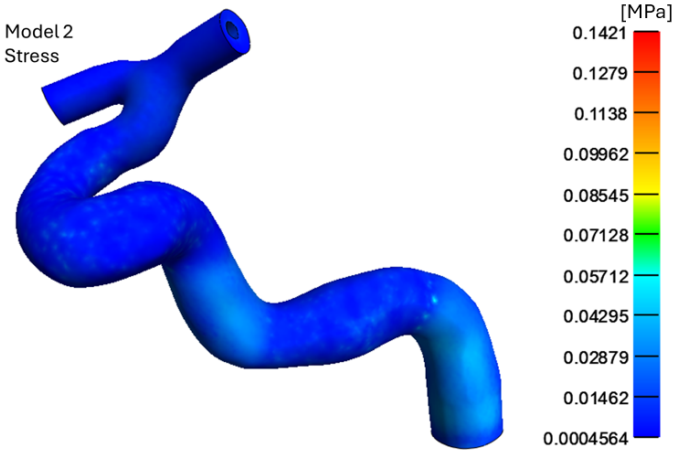

Fig. 20: Stress results for Model 2. Peak stress at t=1s: 0.14 MPa.

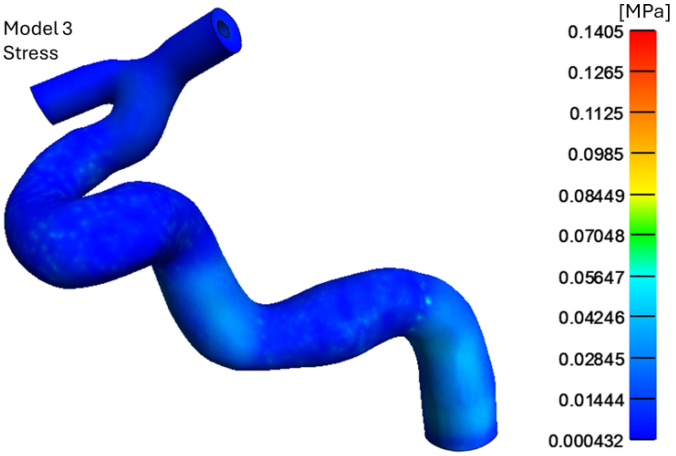

Fig. 21: Stress results for Model 3. Peak stress at t=1s: 0.14 MPa.

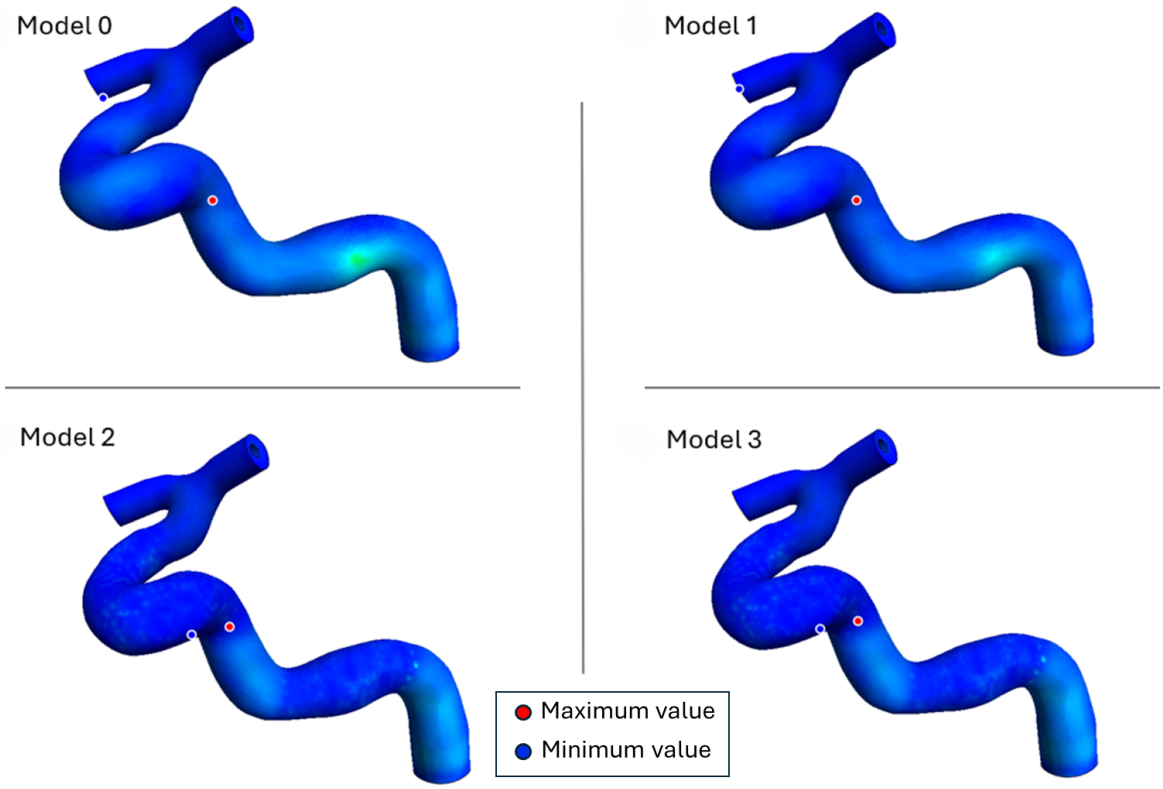

Fig. 22: The location of maximum and minimum stresses across all models, at t=1s.

D. *Effective Lagrange Strain*

The strain results for the four distinct models are shown in Figures 23–26, all evaluated at the terminal time point (1 second). Model 0, with no surrounding tissue, exhibited a peak strain value of 0.28 (Figure 23). Model 1, with soft tissue springs, showed an increased peak strain of 0.32 (Figure 24). Model 2, with bone springs, demonstrated a lower peak strain of 0.19 (Figure 25). Finally, Model 3, which combined both soft tissue and bone springs, presented a peak strain value of 0.19 (Figure 26), almost similar to Model 2.

As for the location of maximum and minimum strains (Figure 27), Models 0 and 1 shared the same maximum strain values but differed in their minimum values. In contrast, Models 2 and 3 exhibited both their minimum and maximum strain values in the same locations.

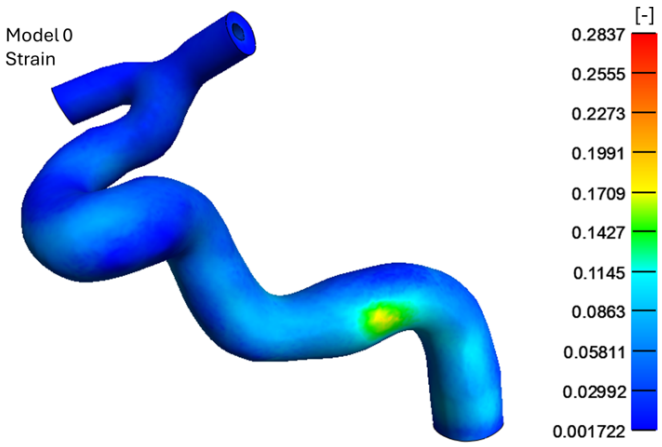

Fig. 23: Strain results for Model 0. Peak strain at t=1s: 0.28.

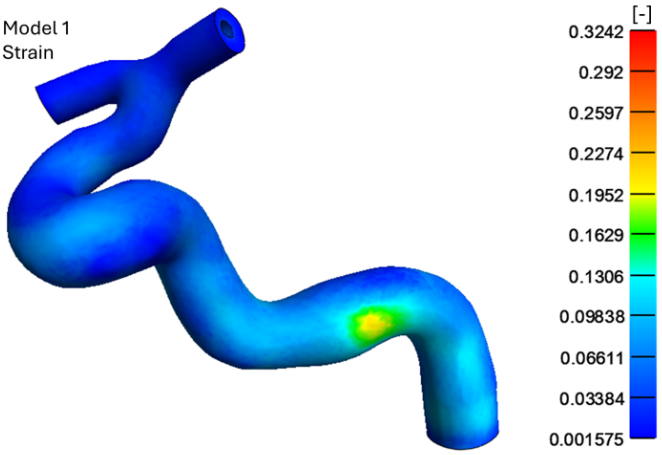

Fig. 24: Strain results for Model 1. Peak strain at t=1s: 0.32.

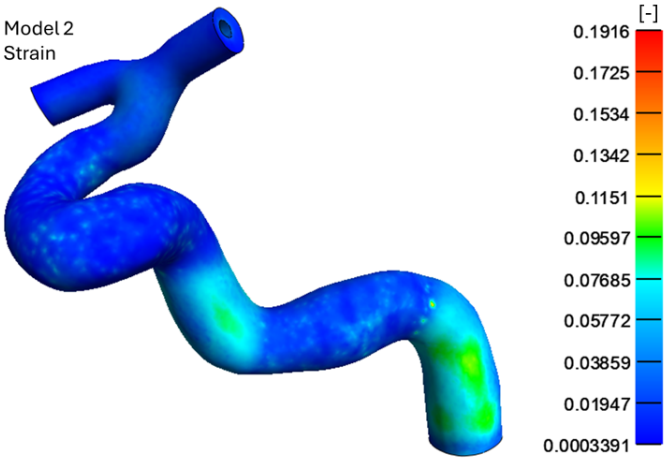

Fig. 25: Strain results for Model 2. Peak strain at t=1s: 0.19.

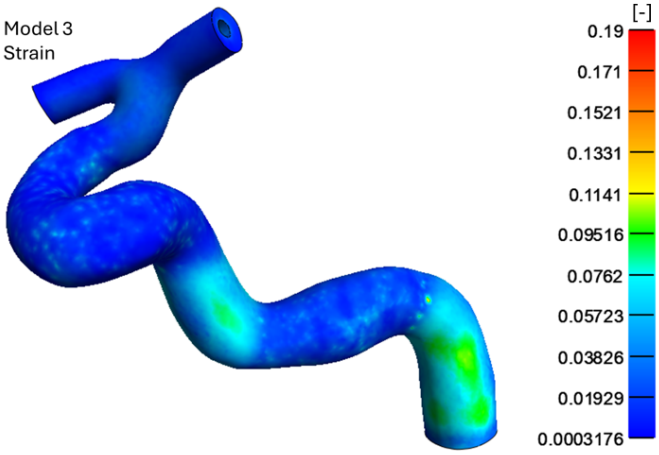

Fig. 26: Strain results for Model 3. Peak strain at t=1s: 0.19.

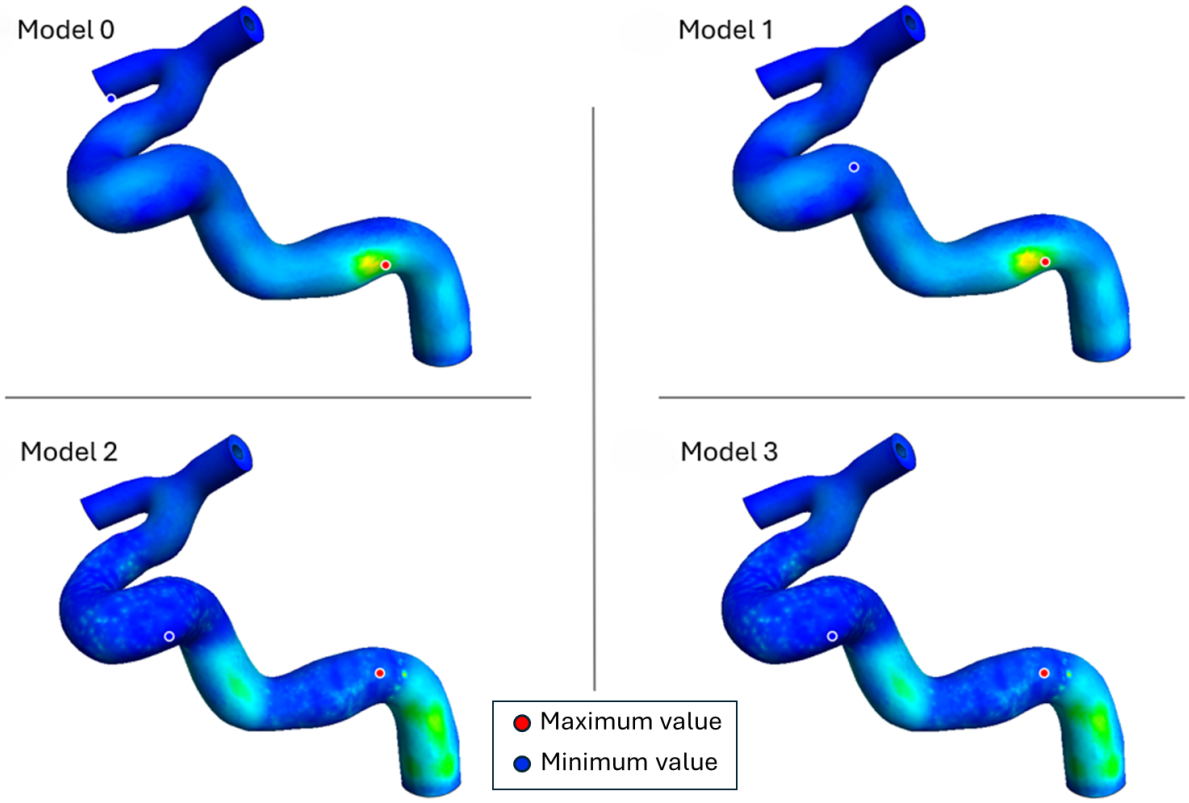

Fig. 27: The location of maximum and minimum strains across all models, at t=1s.

IV. Discussion

This study developed and analyzed four FE models of the ICA to assess the influence of surrounding tissues on simulation outcomes. By systematically incorporating soft tissue and bone interactions, we were able to assess their individual and combined effects on displacement, stress, and strain distributions within the artery.

A. Isolated Artery vs. Individual Tissue Effects

Comparing Model 0 (isolated artery) with Models 1 (soft tissue springs) and 2 (bone springs) reveals the major impact of surrounding tissues on artery mechanics.

1) *Displacement*

The isolated artery model (Model 0) exhibited the highest peak displacement of 0.82 mm. However, adding surrounding tissues led to a significant decrease in displacement, which demonstrates how these tissues provide mechanical support and constraint to the artery. While the inclusion of soft tissue (Model 1) reduced peak displacement by 26.6% compared to the baseline, bone tissue (Model 2) caused a more dramatic 58.4% reduction. This notable decrease in displacement due to bone interaction emphasizes the primary function of rigid anatomical constraints in maintaining arterial stability, which is often overlooked in simplified vascular models.

2) *Stress*

Interestingly, the addition of soft tissue (Model 1) increased peak stress by 17.0% compared to the baseline, while bone tissue (Model 2) slightly decreased it by 5.8%. This unexpected increase in stress levels with the addition of soft tissue indicates that these tissues lead to higher stress within specific regions of the artery, which makes them more prone to damage or remodeling. On the other hand, the presence of bone tissue appears to promote a more uniform stress distribution across the entire structure. These findings imply that bone tissue has a stronger impact on stress distribution than soft tissue.

3) *Strain*

Soft tissue inclusion (Model 1) led to a 14.3% increase in peak strain, whereas bone tissue (Model 2) reduced it by 32.5% compared to the baseline. This divergence showcases the contrasting effects of these tissues on artery deformation. Soft tissues surrounding an artery provide less resistance to arterial deformation due to their inherent flexibility. In contrast, the significant decrease in strain in Model 2 further emphasizes the stabilizing effect of bone on arterial deformation.

Our findings suggest that modeling arteries in isolation tends to exaggerate their movement and deformation. Despite the partial constraint provided by soft tissue, some areas of the artery remain susceptible to higher stress levels, as depicted by Model 1 in Figure 28. In contrast, bone interaction substantially limits arterial movement and distributes stresses more evenly, as shown in Figure 28. This comparison indicates that neglecting the interactions of surrounding tissues, as seen in Model 0's results, leads to overestimated displacements, stresses, and strains. Such overestimation could reduce the accuracy of clinical predictions regarding arterial behavior under physiological and pathological conditions.

B. Individual Tissue Effects

Comparing Model 1 (soft tissue) with Model 2 (bone) allows us to isolate the specific impacts of these tissue types.

1) *Displacement*

The presence of bone tissue reduced peak displacement by 43.3% compared to soft tissue, which demonstrates its superior constraining effect.

2) *Stress*

Model 2 showed a 19.5% lower peak stress than Model 1. This decrease suggests that bone tissue provides a more uniform distribution of forces along the artery.

3) *Strain*

Bone tissue resulted in a 40.9% lower peak strain compared to soft tissue. This huge difference in strain is attributed to the bone's rigid nature.

These results indicate that bone interaction exerts a stronger mechanical constraint on the artery than soft tissue interaction. Bone's rigidity and structural proximity to the ICA likely account for this effect, as the dense composition of bone restricts arterial motion and deformation more than the softer, more flexible tissues do. This outcome is aligned with physiological expectations, as bone, due to its stiffness, creates a firmer boundary condition compared to soft tissues.

Understanding how soft tissue and bone differently influence ICA mechanics is necessary for accurately modeling arterial behavior in specific anatomical regions. Clinically, these findings could guide specific therapeutic treatments and diagnostic assessments, as well as assist surgeons in decision-making based on the dominant tissue interactions present in different parts of the vascular anatomy.

C. Combined vs. Individual Tissue Effects

Comparing Model 3 (combined tissues) with Models 1 and 2 reveals the impact of incorporating both tissue types.

1) *Displacement*

Model 3 showed a 46.1% lower peak displacement than Model 1 and only a 4.9% lower displacement than Model 2. This suggests that bone dominates in constraining artery movement, while soft tissue plays a minor additional role when both are present.

2) *Stress*

The combined model exhibited the lowest peak stress, 20.4% lower than Model 1 and 1.1% lower than Model 2. This indicates that the presence of both tissue types allows for the

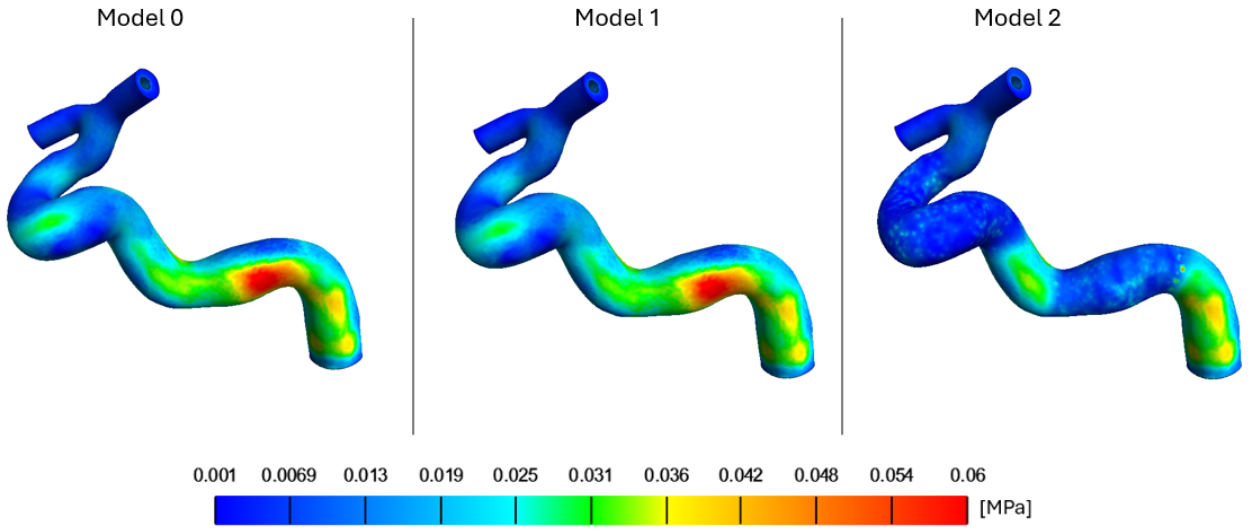

Fig. 28: Stress distribution in the artery across all models, at t=1s.

most efficient distribution of forces, thereby reducing stress in certain areas. However, the marginal improvement over Model 2 (1.1% reduction) implies that Model 2 was already quite effective, but the combined approach still managed to achieve a slight enhancement.

3) *Strain*

Model 3 demonstrated the lowest peak strain, which was 41.4% lower than Model 1 and only 0.8% lower than Model 2. These results reinforce the notion that bone is the primary factor in limiting arterial deformation, while soft tissue contributes minimally in the combined model.

The combination of soft tissue and bone interactions, as seen in Model 3, provides a more comprehensive constraint on the artery, as it captures the natural balance between flexibility and rigidity. This highlights the importance of combining tissue effects for realistic simulations; however, in Model 3, the artery's behavior is primarily influenced by the bone's interaction due to its greater stiffness and strength, while the impact of soft tissues often becomes secondary in regions where bone is present. In clinical modeling and biomechanical simulations, accurately representing bone-artery interfaces and bone geometry is generally more important than modeling detailed soft tissue interactions in various anatomical areas due to the dominant mechanical influence of the bone. Nonetheless, it is important to mention that soft tissue modeling remains essential in specific applications involving regions with little to no bone presence.

D. Limitations and Future Research

This study demonstrates a progressive understanding of the impact of surrounding tissues on ICA modeling. However, several limitations should be acknowledged.

First, the study operates under static conditions and does not incorporate a full FSI approach. Instead, the effects of blood flow are approximated by applying pressure on the inner wall surface of the ICA model, based on loading conditions derived from fluid domain analyses. While FSI was considered unnecessary for the primary focus of this study, it could be relevant in more complex analyses of the ICA in future studies.

Additionally, the simplified representation of surrounding tissues using springs, while adequate for modeling elastic properties, overlooks the viscoelastic behavior of soft tissues. Although this approach is suitable for the arterial wall and bone, which exhibit predominantly elastic characteristics due to negligible viscous effects, it remains uncertain whether such effects would be equally negligible in surrounding soft tissues. Future research should investigate the significance of viscoelastic effects in these tissues and consider implementing dynamic models to more accurately represent their complex biomechanical properties.

Another major drawback is the use of a single case study, which does not account for the anatomical variations in ICA structures among individuals. These variations are usually found in the carotid siphon, at the bifurcation, and in areas where the artery shows increased tortuosity [79]. Despite this limitation, the study's main findings are likely to be applicable across various anatomical structures. The study revealed significant changes in stress, strain, and displacement in the bone region (C2, C3, and C5 segments of the ICA). These insights suggest that similar patterns might occur in other arterial structures among individuals. This assumption requires validation through future research incorporating diverse ICA geometries to confirm the broader relevance of the findings.

Lastly, the impacts of pathological conditions on tissue properties and arterial behavior were not explored. Future research in the context of arterial diseases, could involve adapting these models to mimic pathological conditions like atherosclerosis or aneurysm. This approach could help assess

the influence of tissue interactions on disease progression and treatment outcomes.

It is important to note, however, that while these limitations exist, they do not invalidate the study's findings. Nonetheless, the consequences of these limitations are not yet fully understood. Hence, further exploration in future research is needed to confirm their minimal impact and to uncover any unforeseen effects on arterial mechanics simulations.

V. Conclusion

This study has made significant progress in developing a comprehensive computational model of the ICA that incorporates surrounding tissues. Although our research focused on assessing how surrounding tissue affects computational models of the ICA, it is worth mentioning that our results are specific to one particular ICA geometry and therefore cannot be generalized.

Nevertheless, the methods developed and implemented in this study provide a solid foundation for further research, including the construction of patient-specific model, the incorporation of surrounding tissues, and the application of finite element analysis. Our simulations suggest that incorporating surrounding tissues in ICA models influences simulation outcomes compared to isolated artery models. These commonly used simplified models tend to overestimate arterial displacement and deformation. However, when surrounding tissues are incorporated into the model, they substantially alter the mechanical behavior of the artery. Specifically, the study revealed that the effect of bone tissue on arterial mechanics is more dominant than soft tissue. Furthermore, the combined tissue model (Model 3) provided the most realistic representation and significantly reduced peak displacement, stress, and strain compared to the isolated artery model.

Consequently, these preliminary findings recommend that computational analyses take into account the surrounding environment of the ICA. However, future studies should incorporate multiple patient-specific models and detailed surrounding tissue representations to draw definitive conclusions and improve clinical applications for ICA-related pathologies.

REFERENCES

[1] W. H. Organization, "Cardiovascular diseases kill 10 000 people in the who european region every day, with men dying more frequently than women," May 15 2024, accessed: 2024-10-08. [Online]. Available: https://www.who.int/europe/news/item/15-05-2024-cardiovascular-diseases-kill-10-000-people-in-the-who-european-region-every-day--with-men-dying-more-frequently-than-women

[2] R. Luengo-Fernandez, M. Walli-Attaei, A. Gray, A. Torbica, A. P. Maggioni, R. Huculeci, F. Bairami, V. Aboyans, A. D. Timmis, P. Vardas, and J. Leal, "Economic burden of cardiovascular diseases in the european union: a population-based cost study," *European heart journal*, vol. 44, no. 45, pp. 4752–4767, 2023.

[3] M. Charlick and J. M. Das, "Anatomy, head and neck: Internal carotid arteries," July 2023, accessed: 2024-09-30. [Online]. Available: https://www.ncbi.nlm.nih.gov/books/NBK556061/

[4] C. Krittanawong, J. Escobar, H. U. H. Virk, M. Alam, N. Skeik, U. Campia, P. K. Henke, and S. Sharma, "Carotid and renal vascular disease," *Current Problems in Cardiology*, vol. 49, no. 1, p. 102056, 2024.

[5] L. Wang, A. Maehara, R. Lv, X. Guo, J. Zheng, K. L. Billiar, G. S. Mintz, and D. Tang, "Image-based finite element modeling approach for characterizing in vivo mechanical properties of human arteries," *Journal of Functional Biomaterials*, vol. 13, no. 3, p. 147, 2022.

[6] S. Aslan, X. Liu, E. Chen, M. Mese-Jones, B. Gonzalez, R. O'Hara, Y. Loke, N. Hibino, L. Olivieri, A. Krieger, and T. Nguyen, "Computational modeling of arterial walls: Evaluating model complexity and the influence of model parameters on deformation outcomes," in *SCITEPRESS – Science and Technology Publications, Lda*, 2024.

[7] R. Phellan, B. Hachem, J. Clin, J. Mac-Thiong, and L. Duong, "Real-time biomechanics using the finite element method and machine learning: Review and perspective," *Medical Physics*, vol. 48, no. 1, pp. 7–18, 2020.

[8] E. L. Manchester, D. Roi, B. Gu, X. Y. Xu, and K. Lobotesis, "Modelling combined intravenous thrombolysis and mechanical thrombectomy in acute ischaemic stroke: Understanding the relationship between stent retriever configuration and clot lysis mechanisms," *Life*, vol. 11, no. 11, p. 1271, 2021.

[9] M. Kim, I. Larrabide, M.-C. Villa-Uriol, and A. Frangi, "Hemodynamic alterations of a patient-specific intracranial aneurysm induced by virtual deployment of stents in various axial orientation." *Proceedings - 2009 IEEE International Symposium on Biomedical Imaging: From Nano to Macro, ISBI 2009*, pp. 1215–1218, 06 2009.

[10] M. Fattahi, S. A. Abdollahi, A. H. Alibak, *et al.*, "Influence of parent vessel feature on the risk of internal carotid artery aneurysm rupture via computational method," *Scientific Reports*, vol. 13, p. 20544, 2023.

[11] K. M. Moerman, P. Konduri, B. Fereidoonnezhad, H. Marquering, A. Van Der Lugt, G. Luraghi, S. Bridio, F. Migliavacca, J. F. R. Matas, and P. McGarry, "Development of a patient-specific cerebral vasculature fluid–structure-interaction model," *Journal of Biomechanics*, vol. 133, p. 110896, 2022.

[12] Kenhub, "Internal carotid artery," October 30 2023, accessed: 2024-10-01. [Online]. Available: https://www.kenhub.com/en/library/anatomy/internal-carotid-artery

[13] C. Hacking and J. Jones, "Internal carotid artery," *Radiopaedia.org*, 2008. [Online]. Available: https://doi.org/10.53347/rid-4524

[14] M. Vijaywargiya, R. Deopujari, and S. A. Athavale, "Anatomical study of petrous and cavernous parts of internal carotid artery," *Anatomy & Cell Biology*, vol. 50, no. 3, pp. 163–170, 2017.

[15] D. Sankhla, "Common carotid artery - anatomy, course, branches, function," April 2024, accessed: 2024-09-30. [Online]. Available: https://samarpanphysioclinic.com/common-carotid-artery/

[16] neuroangio.org, "Internal carotid artery and its aneurysms," accessed: 2024-09-30. [Online]. Available: https://neuroangio.org/anatomy-and-variants/internal-carotid-artery-and-its-aneurysms/

[17] S. Bonasia, A. Bouthillier, and T. Robert, "Segmental classification of the internal carotid artery: An overview," *Contemporary Neurosurgery*, vol. 42, no. 18, pp. 1–5, 2020.

[18] A. Bouthillier, H. van Loveren, and J. Keller, "Segments of the internal carotid artery: a new classification," *Neurosurgery*, vol. 38, no. 3, pp. 425–432, March 1996.

[19] M. S. Greenberg, *Handbook of Neurosurgery*, 9th ed. New York: Thieme Medical Publishers Inc, 2020.

[20] S. T. Fernandes, H. L. Dória-Netto, and E. B. Neto, "A new paradigm: How to study the exact location of a paraclinoid aneurysm and the cavernous sinus in the preoperative stage through imaging," in *Advances in Cerebral Aneurysm Treatment*, A. Scerrati and G. Mantovani, Eds. Rijeka: IntechOpen, 2023, ch. 1. [Online]. Available: https://doi.org/10.5772/intechopen.110492

[21] J. J. DePowell, S. C. Froelich, L. A. Zimmer, J. L. Leach, A. Karkas, P. V. Theodosopoulos, and J. T. Keller, "Segments of the internal carotid artery during endoscopic transnasal and open cranial approaches: Can a uniform nomenclature apply to both?" *World Neurosurgery*, vol. 82, no. 6, pp. S66–S71, 2014.

[22] A. Micheau and D. Hoa, "Segments of the internal carotid artery (bouthillier)," October 1 2024, accessed: 2024-10-01. [Online]. Available: https://www.imaios.com/en/e-anatomy/anatomical-structure/segments-of-the-internal-carotid-artery-bouthillier-121133628

[23] I. M. Ziyal, E. Salas, D. C. Wright, and L. N. Sekhar, "The petrolingual ligament: the anatomy and surgical exposure of the posterolateral landmark of the cavernous sinus," *Acta Neurochirurgica (Wien)*, vol. 140, no. 3, pp. 201–204, 1998.

[24] E. Lefevre, C. Apra, S. F. Chodraui-Filho, D. Chauvet, S. Smajda, M. Piotin, and R. Fahed, "Reliability of bony landmarks to predict intradural location of paraclinoid aneurysms," *Clinical Neuroradiology*, vol. 30, no. 4, pp. 843–848, 2020.

[25] A. Harish and A. Harish. (2024, March 14) Finite element method – what is it? fem and fea explained. Accessed: 2024-10-02. [Online]. Available: https://www.simscale.com/blog/what-is-finite-element-method/

[26] B. R. Simon, M. V. Kaufmann, M. A. McAfee, and A. L. Baldwin, "Finite element models for arterial wall mechanics," *Journal of Biomechanical Engineering*, vol. 115, no. 4B, pp. 489–496, 1993.

[27] P. Kalita and R. Schaefer, "Mechanical models of artery walls," *Archives of Computational Methods in Engineering*, vol. 15, no. 1, pp. 1–36, 2007.

[28] A. Erdemir, T. M. Guess, J. Halloran, S. C. Tadepalli, and T. M. Morrison, "Considerations for reporting finite element analysis studies in biomechanics," *Journal of Biomechanics*, vol. 45, no. 4, pp. 625–633, 2012.

[29] M. Hirschhorn, V. Tchantchaleishvili, R. Stevens, J. Rossano, and A. Throckmorton, "Fluid–structure interaction modeling in cardiovascular medicine – a systematic review 2017–2019," *Medical Engineering & Physics*, vol. 78, pp. 1–13, 2020.

[30] A. Valencia, P. Burdiles, M. Ignat, J. Mura, E. Bravo, R. Rivera, and J. Sordo, "Fluid structural analysis of human cerebral aneurysm using their own wall mechanical properties," *Computational and Mathematical Methods in Medicine*, vol. 2013, p. 293128, 2013, epub 2013 Sep 18. PMID: 24151523; PMCID: PMC3789306.

[31] M. Kizhisseri, S. Gharaie, S. R. Boopathy, *et al.*, "Differential sensitivities to blood pressure variations in internal carotid and intracranial arteries: a numerical approach to stroke prediction," *Scientific Reports*, vol. 13, p. 22319, 2023.

[32] N. Curcio, A. Rosato, D. Mazzaccaro, *et al.*, "3d patient-specific modeling and structural finite element analysis of atherosclerotic carotid artery based on computed tomography angiography," *Scientific Reports*, vol. 13, p. 19911, 2023.

[33] A. J. Oyejide, A. A. Awonusi, and E. O. Ige, "Fluid-structure interaction study of hemodynamics and its biomechanical influence on carotid artery atherosclerotic plaque deposits," *Medical Engineering Physics*, vol. 117, p. 103998, 2023.

[34] M. T. B. Truijman, M. E. Kooi, A. C. Van Dijk, A. a. J. De Rotte, A. G. Van Der Kolk, M. I. Liem, F. H. B. M. Schreuder, E. Boersma, W. H. Mess, R. J. Van Oostenbrugge, P. J. Koudstaal, L. J. Kappelle, P. J. Nederkoorn, A. J. Nederveen, J. Hendrikse, A. F. W. Van Der Steen, M. J. a. P. Daemen, and A. Van Der Lugt, "Plaque at risk (parisk): Prospective multicenter study to improve diagnosis of high-risk carotid plaques," *International Journal of Stroke*, vol. 9, no. 6, pp. 747–754, 2013.

[35] G. Code, "ggremesh," n.d., available online at: https://www.gibboncode.org/html/HELP_ggremesh.html.

[36] S. C. Tadepalli, A. Erdemir, and P. R. Cavanagh, "Comparison of hexahedral and tetrahedral elements in finite element analysis of the foot and footwear," *Journal of Biomechanics*, vol. 44, no. 12, pp. 2337–2343, 2011.

[37] F. Alkhatib, G. Bourantas, A. Wittek, and K. Miller, "Generation of patient-specific structured hexahedral mesh of aortic aneurysm wall," in *Computational Biomechanics for Medicine*, M. Nash, A. Wittek, P. Nielsen, M. Kobielarz, A. Babu, and K. Miller, Eds. Springer, Cham, 2023.

[38] N. Zaman, M. Ferdows, M. Xenos, K. Hoque, and E. Tzirtzilakis,

"Effect of angle bifurcation and stenosis in coronary arteries: An idealized model study," *BioMed Research Journal*, vol. 4, no. 2, pp. 220–234, 2021.

[39] P. Lamata, S. Niederer, D. Nordsletten, D. C. Barber, I. Roy, D. R. Hose, and N. Smith, "An accurate, fast and robust method to generate patient-specific cubic hermite meshes," *Medical Image Analysis*, vol. 15, no. 6, pp. 801–813, 2011.

[40] H. Si, "Tetgen, a quality tetrahedral mesh generator and a 3d delaunay triangulator, version 1.5, user's manual," Weierstrass Institute for Applied Analysis and Stochastics (WIAS), Tech. Rep. Tech. Rep. 13, 2013.

[41] WIAS Software, "Tetgen, a quality tetrahedral mesh generator and a 3d delaunay triangulator," https://wias-berlin.de/software/index.jsp?id=TetGen&lang=1, n.d., accessed: 2024-10-05.

[42] K. M. Moerman, "GIBBON: The Geometry and Image-Based Bioengineering add-On," *Journal of Open Source Software*, vol. 3, no. 22, p. 506, 2018. [Online]. Available: https://doi.org/10.21105/joss.00506

[43] Febio, "Febio software suite," 2017, available online at: https://febio.org/.

[44] S. A. Maas, B. J. Ellis, G. A. Ateshian, and J. A. Weiss, "Febio: Finite elements for biomechanics," *Journal of Biomechanical Engineering*, vol. 134, no. 1, p. 011005, 2012.

[45] Q. T. U. Welsim, "Neo-hookean hyperelastic model for nonlinear finite element analysis," *Medium*, December 2021. [Online]. Available: https://getwelsim.medium.com/neo-hookean-hyperelastic-model-for-nonlinear-finite-element-analysis-16ac996aa507

[46] W. J. A. G. Maas S., Herron M., "Neo-hookean hyperelasticity," FEBio Documentation, accessed: 2024-10-02. [Online]. Available: https://help.febio.org/docs/FEBioTheory-3-6/TM36-Subsection-5.2.3.html

[47] Toppr Guides. (2020, July 15) Hooke's law and stress-strain curve: analysis, videos and examples. Accessed: 2024-10-02. [Online]. Available: https://www.toppr.com/guides/physics/mechanical-properties-of-solids/hookes-law-and-stress-strain-curve/#:~:text=Or%2C%20Stress%20%3D%20k%20%C3%97%20Strain,is%20valid%20for%20most%20materials

[48] T. E. of Encyclopaedia Britannica. (1998, July 20) Elasticity — definition, examples, & facts. Accessed: 2024-10-02. [Online]. Available: https://www.britannica.com/science/elasticity-physics

[49] B. Kim, S. B. Lee, J. Lee, S. Cho, H. Park, S. Yeom, and S. H. Park, "A comparison among neo-hookean model, mooney-rivlin model, and ogden model for chloroprene rubber," *International Journal of Precision Engineering and Manufacturing*, vol. 13, no. 5, pp. 759–764, 2012.

[50] D. P. Rosen and J. Jiang, "A comparison of hyperelastic constitutive models applicable to shear wave elastography (swe) data in tissue-mimicking materials," *Physics in Medicine and Biology*, vol. 64, no. 5, p. 055014, 2019.

[51] S. Marchesseau, S. Chatelin, and H. Delingette, "Nonlinear biomechanical model of the liver," in *Elsevier eBooks*. Elsevier, 2017, pp. 243–265.

[52] M. J. Lohr, G. P. Sugerman, S. Kakaletsis, E. Lejeune, and M. K. Rausch, "An introduction to the ogden model in biomechanics: benefits, implementation tools and limitations," *Philosophical Transactions of the Royal Society A: Mathematical, Physical and Engineering Sciences*, vol. 380, no. 2234, p. 20210365, October 2022.

[53] Q. T. U. Welsim, "Ogden hyperelastic model for nonlinear finite element analysis," https://getwelsim.medium.com/ogden-hyperelastic-model-for-nonlinear-finite-element-analysis-df9518de3b48, December 2021, accessed: 2024-10-02.

[54] G. Youssef, "Chapter 5 - hyperelastic behavior of polymers," in *Applied Mechanics of Polymers*, G. Youssef, Ed. Elsevier, 2022, pp. 117–144. [Online]. Available: https://www.sciencedirect.com/science/article/pii/B9780128210789000028

[55] K. N. Nieto Taborda, C. Wilches, A. Manrique, Radiology, B. C. Diagnostic Imaging Resident, Fundacion Universitaria Sanitas, C. R. S. Neuroradiologist, Department of Radiology, F. U. S. B. C. Residents, Teaching Assistant, C. R. S. Radiologist, Department of Radiology, and B. C. Teaching Assistant, Fundacion Universitaria Sanitas, "A diagnostic algorithm for patients with intracranial calcifications," *Revista Colombiana de Radiología*, vol. 28, no. 3, pp. 4732–4739, 2017. [Online]. Available: http://contenido.acronline.org/Publicaciones/RCR/RCR28-3/04-RCR-28-3-Algoritmos_Ingles%20(para%20publicacion).pdf

[56] S. D. Williamson, Y. Lam, H. F. Younis, H. Huang, S. Patel, and R. D. Kamm, "On the sensitivity of wall stresses in diseased arteries to variable material properties," *Journal of Biomechanical Engineering*, vol. 125, no. 1, pp. 147–155, 2003.

[57] N. L. Henry, P. D. Shah, I. Haider, P. E. Freer, R. Jagsi, and M. S. Sabel, "Cancer of the breast," in *Elsevier eBooks*. Elsevier, 2020, pp. 1560–1603.e12.

[58] W. J. A. G. Maas S., Herron M., "Mooney-rivlin," FEBio Documentation, accessed: 2024-10-05. [Online]. Available: https://help.febio.org/docs/FEBioUser-4-7/UM47-4.1.2.9.html

[59] K. L. Monson, N. M. Barbaro, and G. T. Manley, "Biaxial response of passive human cerebral arteries," *Annals of Biomedical Engineering*, vol. 36, pp. 2028–2041, 2008.

[60] K. M. Moerman, C. K. Simms, and T. Nagel, "Control of tension–compression asymmetry in ogden hyperelasticity with application to soft tissue modelling," *Journal of the Mechanical Behavior of Biomedical Materials*, vol. 56, pp. 218–228, 2015.

[61] S. Lu and S. Zhang, "Atherosclerosis research: the impact of physiological parameters on vascular wall stress," *SN Applied Sciences*, vol. 1, p. 692, 2019.

[62] FEBio Documentation, "Section 3.11 the curve editor," FEBio Documentation, n.d., accessed: 2024-11-10. [Online]. Available: https://help.febio.org/FEBioStudio/FEBioStudio_1-5-Section-3.11.html

[63] J. Gade, "Mechanical properties of arteries: Identification and application," Thesis, Linköping University, 2019.

[64] P. Moireau, N. Xiao, M. Astorino, C. A. Figueroa, D. Chapelle, C. A. Taylor, and J. F. Gerbeau, "External tissue support and fluid-structure simulation in blood flows," *Biomechanics and Modeling in Mechanobiology*, vol. 11, no. 1-2, pp. 1–18, 2012.

[65] B. Wu, C. Shu, and M. Wan, "An implicit immersed boundary method for robin boundary condition," *International Journal of Mechanical Sciences*, vol. 261, p. 108694, 2023.

[66] E. F. Morgan, G. U. Unnikrisnan, and A. I. Hussein, "Bone mechanical properties in healthy and diseased states," *Annual Review of Biomedical Engineering*, vol. 20, pp. 119–143, 2018.

[67] J. D. Humphrey, "Biological soft tissues," in *Springer Handbook of Experimental Solid Mechanics*, W. Sharpe, Ed. Boston, MA: Springer, 2008, pp. 185–217.

[68] M. G. Dunn and F. H. Silver, "Viscoelastic behavior of human connective tissues: relative contribution of viscous and elastic components," *Connective Tissue Research*, vol. 12, no. 1, pp. 59–70, 1983.

[69] J. P. Mynard, A. Kondiboyina, R. Kowalski, M. M. H. Cheung, and J. J. Smolich, "Measurement, analysis and interpretation of pressure/flow waves in blood vessels," *Frontiers in Physiology*, vol. 11, p. 1085, 2020.

[70] L. Failer, P. Minakowski, and T. Richter, "On the impact of fluid structure interaction in blood flow simulations," *Vietnam Journal of Mathematics*, vol. 49, pp. 169–187, 2021.

[71] A. Redaelli and E. Votta, "Cardiovascular patient-specific modeling: Where are we now and what does the future look like?" *APL Bioengineering*, vol. 4, no. 4, 2020.

[72] Taylor Francis, "Anterior clinoid process - knowledge and references," https://taylorandfrancis.com/knowledge/Medicine_and_healthcare/Anatomy/Anterior_clinoid_process/, accessed: 2024-10-30.

[73] J. T. Keller, H. R. Van Loveren, A. N. Sepahi, and M. Zuccarello, "Internal carotid artery: correlative anatomy as a guide to surgery," *International Congress Series*, vol. 1247, pp. 3–18, 2002.

[74] J. M. Kim, A. Romano, A. Sanan, H. R. Van Loveren, and J. T. Keller, "Microsurgical anatomic features and nomenclature of the paraclinoid region," *Neurosurgery*, vol. 46, no. 3, pp. 670–682, 2000.

[75] FEBio User Manual, "List of plotfile variables," n.d. [Online]. Available: https://help.febio.org/docs/FEBioUser-3-6/UM36-3.18.2.2.html

[76] FEBio Documentation, "5.6.5.4 von mises stress," FEBio Documentation, n.d., accessed: 2024-11-10. [Online]. Available: https://help.febio.org/docs/FEBioTheory-3-6/TM36-5.6.5.4.html

[77] FEBio Theory Manual, "Subsection 2.3.3 stress," n.d., accessed: 2024-11-10. [Online]. Available: https://help.febio.org/FEBioTheory/FEBio_tm_3-4-Subsection-2.3.3.html

[78] FEBio Documentation. (n.d.) Subsection 2.3.2 strain. Accessed: 2024-11-10. [Online]. Available: https://help.febio.org/docs/FEBioTheory-3-6/TM36-Subsection-2.3.2.html

[79] S. Johnson, A. Dwivedi, M. Mirza, R. McCarthy, and M. Gilvarry, "A review of the advancements in the in-vitro modelling of acute ischemic stroke and its treatment," *Frontiers in Medical Technology*, vol. 4, 2022.